JOURNAL OF SPACECRAFT AND ROCKETS
Vol. 36, No. 2, March–April 1999

Numerical Investigation of Shock/Vortex Interaction in Hypersonic Thermochemical Nonequilibrium Flow

Satoru Yamamoto* and Norinao Takasu†
Tohoku University, Sendai 980-8579, Japan
and
Hideo Nagatomo‡
Osaka University, Osaka 565, Japan

A numerical investigation of unsteady hypersonic shock/shock interference flows classified by Edney (Edney, B. E., "Anomalous Heat Transfer and Pressure Distributions on Blunt Bodies at Hypersonic Speeds in the Presence of an Impinging Shock," Aeronautical Research Inst. of Sweden, FFA Rept. 115, Stockholm, Sweden, Feb. 1968) considering the thermochemical nonequilibrium effect is presented. The numerical method used is composed of the fourth-order compact MUSCL total variational diminishing scheme, the maximum second-order lower–upper symmetric Gauss–Seidel scheme, and the advection upstream splitting method scheme for capturing shocks and vortices accurately. The two-temperature model based on the Park model (Park, C., "Two-Temperature Interpretation of Dissociation Rate Data for N_2 and O_2," AIAA Paper 88-0458, Jan. 1988) has taken the thermochemical nonequilibrium into consideration. The nitrogen flows under several flow conditions are calculated. The obtained results show that the type of the shock/shock interference is strongly dependent on the location of the impinging shock as well as the shock standoff distance. Finally, unsteady flow characteristics associated with the thermochemical nonequilibrium effect, especially very complicated flow structures involving shocks, compression waves, vortices, and their interactions, are investigated and explained.

Nomenclature

C_{vs} = translational specific heat of species s
E = total internal energy per unit volume
E_v = vibrational energy per unit volume
F_i = flux, where i is 1, 2
$\boldsymbol{H}$ = vector of source term
h_s = enthalpy per unit mass of species s
h_s^0 = heat of formation of species s
M_s = atomic weight of species s
m = number of diatomic species
n = number of species
p = static pressure
$\boldsymbol{Q}$ = vector of unknown variables
q_j = translational–rotational heat conductions, where j is 1, 2
q_{vj} = vibrational heat conductions, where j is 1, 2
R = universal gas constant
$\boldsymbol{S}$ = vector of diffusion term
T = translational–rotational temperature
t = time
U_i = contravariant velocities, where i is 1, 2
u_i = physical velocities, where i is 1, 2
v_{sj} = diffusion velocities of species s, where j is 1, 2
ξ_i = general curvilinear coordinates, where i is 1, 2
ρ = total density
ρ_s = density of species s
τ_{ij} = shear stress tensor, where i, j are 1, 2

Introduction

HYPERSONIC shock/shock interference flows might be the most complicated flow problems that appear around the hypersonic vehicle. Edney[1] classified them into six types. The most critical case, type IV, has been already studied experimentally by a number of researchers.[2–4] In this type, a supersonic jet generated from the interference point between an impinging shock and a bow shock stagnates on the body surface, and the induced small bow shock, the so-called jet bow shock, causes an extremely significant stagnation heating. Hains and Keyes[2] investigated the shock heating experimentally. Wieting and Holden[3] reported that the flow is very sensitive to flow conditions, such as the inlet Mach number, the impinging shock angle, and the Reynolds number. Holden and Kolly[4] indicated that the supersonic jet is self-oscillating at a finite degree of angle. This result suggests that type IV must be an unsteady interaction. However, more detailed investigations, for example, of unsteady flow characteristics, have not as yet been reported by experimental studies.

However, recent computational fluid dynamics (CFD) approaches[5–7] have investigated unsteady flow characteristics associated with the unsteady supersonic jet. Lind and Lewis[5] investigated the unsteadiness depending on the impinging shock location. Zhong[6] demonstrated that the periodical oscillation of the supersonic jet induces unsteady supersonic shear layers along the body surface. Yamamoto and Kano[7] reported that periodical compression waves are generated from the stagnation point of the jet. The wave propagates in the subsonic region behind the bow shock, and a contact discontinuity is produced due to the interaction with the bow shock. Finally, a number of contact discontinuities further interact with forthcoming compression waves. Therefore, we believe that the type IV case involves significant unsteady and complicated flow characteristics associated with shock/shock interference.

The present study investigates shock/shock interference flows at the high temperature. In general, the thermochemical nonequilibrium effect due to molecular dissociations and vibrations is a relative decrease of the shock standoff distance. Kortz et al.[8] and Hornung et al.[9] reported experimental studies for high-enthalpy shock/shock interference flow. It was observed in both studies that the decrement of the shock standoff distance deforms the type of the shock/shock interference. Those results also suggest that high-enthalpy flows must be unsteady, too. A few numerical studies have also been reported.[10–12] Hannemann et al.[10] demonstrated the deformation of the type of shock interference according to the decrease of the shock standoff distance. However, only a steady-state solution was obtained. Furumoto et al.[11] successfully obtained an unsteady flow of type IV shock interference using the second-order total variational diminishing (TVD) scheme and the third-order semi-implicit

Received July 5, 1997; revision received Oct. 15, 1998; accepted for publication Nov. 9, 1998.

*Associate Professor, Department of Aeronautics and Space Engineering. Member AIAA.
†Graduate Student, Graduate School of Engineering.
‡Research Associate, Institute of Laser Engineering. Member AIAA.

Runge–Kutta scheme. Nagatomo et al.[12] proposed an efficient CFD approach for investigating unsteady flow characteristics of the shock interference associated with the thermochemical nonequilibrium effect.

A lot of numerical studies have already been reported with regard to the numerical method of thermochemcial nonequilibrium flows. Gnoffo[13] developed a CFD code based on the point implicit relaxation method. Candler and MacCormack[14] calculated thermochemical nonequilibrium flows considering each vibrational temperature for molecular species. Park and Yoon[15] employed the fully coupled implicit method to accelerate the convergence of solution. Park[16,17] proposed thermochemcial nonequilibrium models for the chemical reaction and the molecular vibration. Those models are widely used in recent studies. In them, a two-temperature model composed of a translational-rotational temperature and a vibrational-electron temperature is defined.

In the present paper, a parametric study for hypersonic shock/shock interference flows with and without chemical reaction is presented. The influence of the impinging shock location and the temperature is investigated using two CFD approaches: the shock/shock interference flow solver with nonreaction (SSNR)[7] and the shock/shock interference flow solver with reaction (SSR).[12] Ideal gas flows without chemical reaction at low temperature are calculated using the SSNR, and nitrogen flows at high temperature are calculated using the SSR. The SSR employs the two-temperature Park model[17] for solving thermochemical nonequilibrium flows. The numerical method used in the SSR is fundamentally similar to the SSNR. The advection upstream splitting method (AUSM)_DV scheme[18] is newly employed for improving the stability of the calculation. The diagonal point implicit scheme[19] is additionally applied to the maximum second-order lower–upper symmetric Gauss–Seidel (LU-SGS) scheme[7] for calculating the source terms of the species continuity equations and the vibrational energy equation. The transition type of the shock interference due to the changes of the impinging shock location and the temperature is demonstrated using the SSNR and the SSR.

The other purpose of the present paper is to understand unsteady flow characteristics associated with the thermochemical nonequilibrium effect. The present study focuses on whether the unsteady flow characteristics that appear in the nonreaction case, such as unsteady supersonic shear layers, compression waves, and contact discontinuities, are also seen in the reaction case.

Finally, the unsteady vortical supersonic jet comprising shocklets, compression waves, vortices, and their interactions that is obtained in the present reaction case is qualitatively explained as a typical flow characteristic due to the thermochemical nonequilibrium effect.

Fundamental Equations

The fundamental equations in general curvilinear coordinates for solving the hypersonic two-dimensional shock/shock interference flow with the thermochemical nonequilibrium effect contain species continuity equations, momentum equations, a total energy equation, and a vibrational energy equation. Ionization and radiation are neglected. Flows are assumed to be laminar. The equations are written in vector form as

$$\frac{\partial \boldsymbol{Q}}{\partial t} + \frac{\partial F_i}{\partial \xi_i} + \boldsymbol{S} + \boldsymbol{H} = 0 \tag{1}$$

where

$$\boldsymbol{Q} = J\begin{bmatrix} \rho_s \\ \rho u_1 \\ \rho u_2 \\ E \\ E_v \end{bmatrix}, \qquad F_i = J\begin{bmatrix} \rho_s U_i \\ \rho u_1 U_i + \dfrac{\partial \xi_i}{\partial x_1} p \\ \rho u_2 U_i + \dfrac{\partial \xi_i}{\partial x_2} p \\ (E+p)U_i \\ E_v U_i \end{bmatrix}, \qquad \boldsymbol{S} = -J\frac{\partial \xi_i}{\partial x_j}\frac{\partial}{\partial \xi_i}\begin{bmatrix} -\rho_s v_{sj} \\ \tau_{1j} \\ \tau_{2j} \\ \tau_{\ell j} u_\ell - q_j - \displaystyle\sum_{s=1}^{n} \rho_s v_{sj} h_s \\ -q_{vj} - \displaystyle\sum_{s=1}^{m} \rho_s e_{vs} v_{sj} \end{bmatrix}, \qquad \boldsymbol{H} = -J\begin{bmatrix} w_s \\ 0 \\ 0 \\ 0 \\ W_v \end{bmatrix}$$

$$(s = 1, \ldots, n,\ i = 1, 2)$$

Models for chemical reactions and molecular vibrations in the source term H are mainly quoted from the two-temperature model by Park.[17] The viscosity model and the diffusion velocity model are based on the work of Blottner et al.[20] and Lee.[21] The total energy E and the pressure p are

$$E = \sum_{s=1}^{n} \rho_s C_{vs} T + \frac{1}{2}\rho u_j u_j + E_v + \sum_{s=1}^{n} \rho_s h_s^0$$

$$p = \sum_{s=1}^{n} \rho_s \frac{R}{M_s} T$$

Numerical Methods

The numerical schemes employed for the SSR are fundamentally the same as for the SSNR. The SSNR based on the finite difference method is concisely explained here.

1) The modified AUSM scheme[7] is used for the flux splitting. It is known that the original AUSM scheme[22] fails to capture the strong bow shock. In the modified one, the original AUSM algorithm is replaced by the Hänel scheme at the bow shock location monitoring the pressure gradient. The unsteady bow shocks of the type IV shock interference were successfully captured in previous work.[7]

2) The maximum second-order LU-SGS scheme,[7] coupled with the Newton iteration and the Crank–Nicholson method, is used for the time integration to obtain time-accurate solutions.

3) The fourth-order compact MUSCL TVD (FCMT) scheme[23] is applied to the modified AUSM for the higher-order approximation of the primitive variables.

The SSR employs the same schemes except for the modified AUSM scheme. The AUSM_DV scheme[18] is newly employed to improve the stability of the calculation for thermochemical nonequilibrium flows. The diagonal point implicit scheme[19] is also used for the calculation of the source term in Eq. (1).

Initial and Boundary Conditions

All cases begin with the calculation of the initial condition for the unsteady flow calculation. The impinging shock conditions at the inlet boundary and the uniform flow conditions at inner points are specified. The impinging shock condition is calculated from the Rankin–Hugoniot relation. The molecular dissociation behind the impinging shock is not considered because it can be assumed as negligible. None of Newton iterations are executed until the initial condition are obtained. When the calculated shock standoff distance locates an estimated proper point, a few Newton iterations (usually three) are started. The outlet boundary condition is treated as the supersonic outlet flow. Then the inner upstream values are extrapolated. No-slip and adiabatic conditions are specified at the solid wall boundary. The fully catalytic wall is also used for reaction cases.

Computational Grids

In this paper, the impinging shock location is changed parametrically. A computational grid is set up algebraically for each case. Figure 1 shows one of the grids. Grid refinement may be very

Fig. 1 Computational grid, 271 × 171 points.

important if unsteady flow characteristics are to be obtained accurately. The grid points are clustered at the shock location in both the ξ and η directions for higher resolution. The grid points employed are determined for capturing compression waves accurately in thermochemical nonequilibrium flows, as will be shown later.

Results

Nonreaction Cases

The shock/shock interference flows without chemical reaction are calculated first. The flow conditions are almost the same as in Ref. 7 except for the location of the impinging shock. The main flow conditions that are specified are a Mach number of 8.03, temperature of 111.56 K, and pressure of 985.01 Pa, and the flow direction is 0 deg as the uniform inlet boundary condition. The flow angle behind the impinging shock is fixed at 12.5 deg. The Reynolds number is 5.15×10^5. The flow conditions and typical flow characteristics already known are summarized in Fig. 2. Parameters θ and ψ are defined in Fig. 2. The unsteady flow characteristics already obtained[7] are summarized in Fig. 3. Seven different locations of the impinging shock from $\theta = -11$ to 15 deg are studied. Before the main calculation, the accuracy of the modified AUSM scheme is compared with that of the AUSM_DV scheme in some nonreaction cases. Conclusively, the instantaneous temperature contours obtained with both schemes were almost the same in the present cases. Therefore, the modified AUSM scheme is employed for the nonreaction cases to save the CPU time slightly.

Figures 4a–4c show the calculated instantaneous temperature contours for $\theta = -11$, 0, and 15 deg. Typical type IV shock/shock interference is seen in the results for $\theta = 0$ and 15 deg, whereas that of $\theta = -11$ deg results in type III. Unsteady and complicated flow characteristics, especially vortical supersonic shear layers, are captured in all three cases. A similar characteristic of the interaction between compression waves and contact discontinuities shown in Fig. 3 is found for $\theta = 0$ and 15 deg. Some complicated shocklet/vortex interactions in the supersonic shear layer are also found for $\theta = 15$ deg.

Figure 5 shows the time-averaged maximum pressure ratios at the stagnation point of the supersonic jet for the case of six impinging shock locations at $\theta = -11$, -7, -5, 0, 7, and 15 deg, as well as the experimental data.[3] The error bars indicate the time-averaged maximum and minimum values of the ratios. The ratios may be well evaluated because the experimental data are located within the length of error bars. The value of θ indicating the transition point of the shock/shock interference type from type IV to type III is located at $-7 < \theta < -5$ deg.

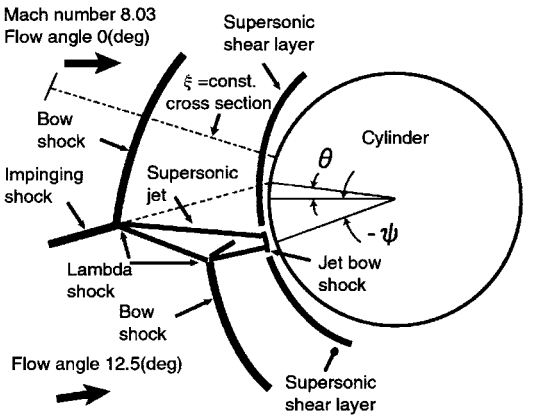

Fig. 2 Shock/shock interference flow and definition of parameters.

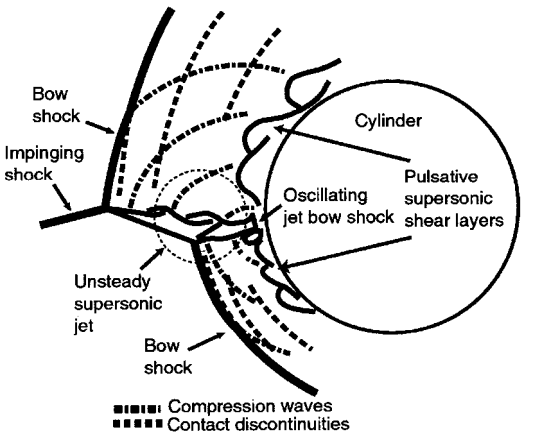

Fig. 3 Unsteady flow characteristics in type IV shock/shock interference.[7]

Reaction Cases

The shock/shock interference flows with the thermochemical nonequilibrium effect are next studied. A partially dissociated nitrogen flow in which the mass fraction of N_2 and N is specified as 95.4% and 0.46% is considered. The flow conditions of the uniform inlet Mach number, the flow direction, and the impinging shock angle are fixed as in the nonreaction case. The uniform inlet translational-rotational temperature is specified by 800 K (Ref. 11), and the Reynolds number is 7×10^4. A lower Reynolds number is set to avoid the turbulence effect as much as possible because the flow is assumed to be laminar. Because a turbulence model might be necessary to evaluate the heat flux in the boundary layer accurately, no evaluation of the heat flux is done in this paper. Three cases of the impinging shock location, $\theta = -11$, 0, and 15 deg, are calculated.

The numerical accuracy of the SSR code was checked with regard to the shock standoff distance in typical hypersonic thermochemical nonequilibrium flows around a sphere[24] and a cylinder.[25] The former case with inlet Mach number of 15.3 results in a 5% difference,[26] and the latter case with inlet Mach number of 6.14 and Reynolds number of 12×10^4 results in a 7% difference with the experiment. Because both cases agree with the experiments within a 10% error, flow characteristics, especially the stagnation location of the supersonic jet, are well captured. In addition, the numerical accuracy of the grid has been checked before the main calculations. Figures 6a and 6b show the calculated instantaneous translational–rotational temperature contours at $\theta = 0$ deg. The grids used have 141×91 (coarse) and 211×141 (medium) grid points, respectively. The present study is focused on unsteady flow characteristics, such as shocks, vortices, compression waves, and their interactions. The coarse grid case does not seem to capture them accurately. The medium grid case could improve the resolution; however, compression waves could not be captured completely when compared to the fine case shown in Fig. 7b. Therefore, a much finer grid (271×171 points) is finally employed.

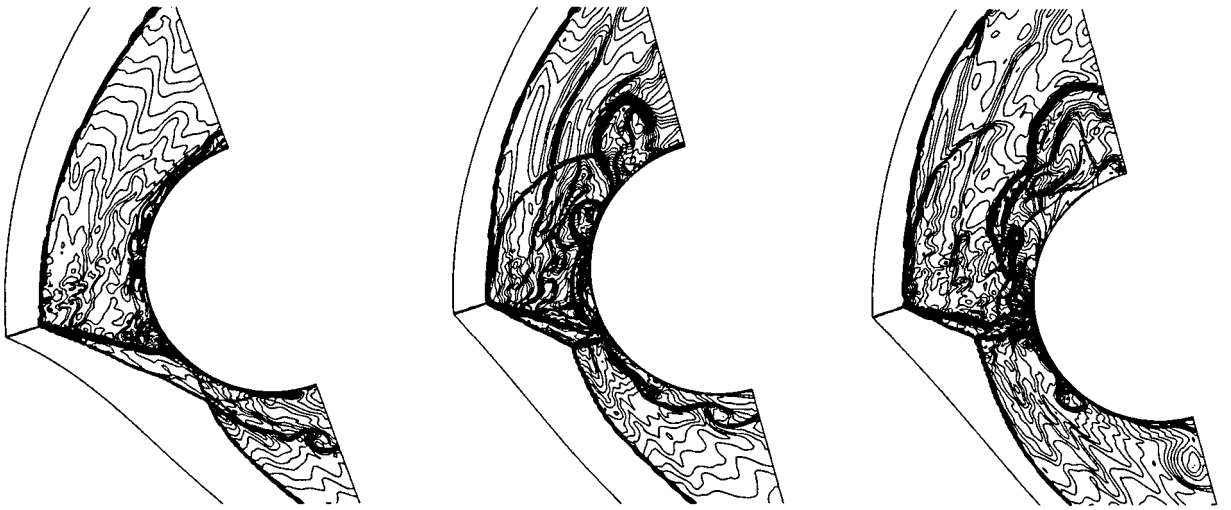

a) $\theta = -11$ deg b) $\theta = 0$ deg c) $\theta = 15$ deg

Fig. 4 Instantaneous temperature contours.

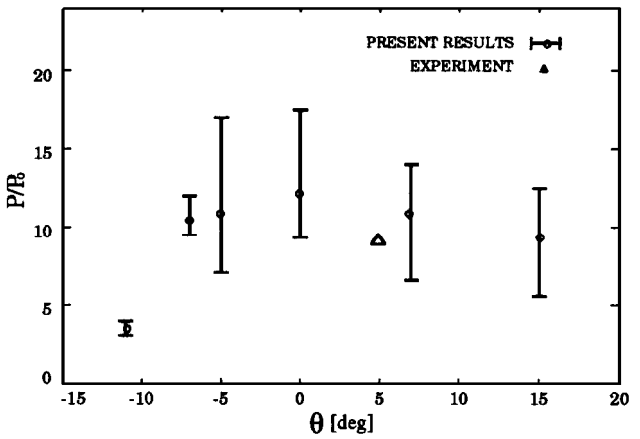

Fig. 5 Time-averaged maximum pressure ratios at the stagnation point of the supersonic jet.

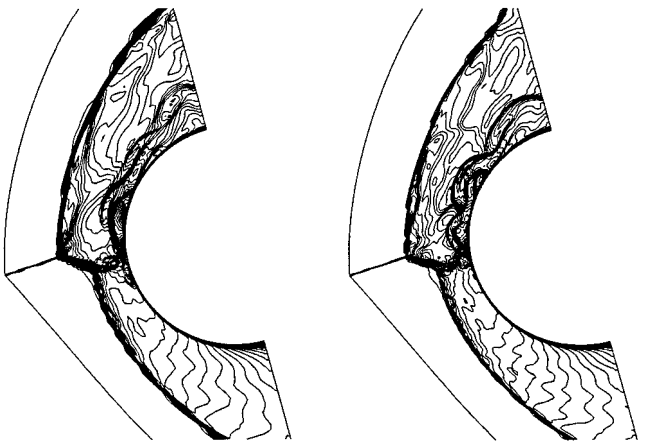

a) 141 × 91 grid points b) 211 × 141 grid points

Fig. 6 Instantaneous temperature contours.

Figures 7a–7c show the instantaneous translational-rotational temperature contours for $\theta = -11$, 0, and 15 deg, respectively. Figures 7a–7c can be compared with Figs. 4a–4c. The shock standoff distance considerably decreases in every reaction case. The flow pattern of type III at $\theta = -11$ deg in Fig. 4a transforms into type IV in Fig. 7a, whereas type IV at $\theta = 15$ deg in Fig. 4c transforms into an unknown type in Fig. 7c. The unknown type is similar to type V. However, none of typical shock reflections behind the jet in type V is observed, and the jet in the present result is much thicker than that expected in type V. Therefore, it should be a new type. We call it type VII here.

The time history of the maximum pressure ratio on the body surface in the case of $\theta = -11$ deg that forms type IV is plotted in Fig. 8. It is found that the stagnation pressure of the supersonic jet is complexly changed in the present reaction case. Figure 9 shows the time history of the pressure ratio distributions on the body surface. The stagnation pressure p_0 is obtained directly from the calculation without the impinging shock. The highest peak values coincide with those at the stagnation point. The maximum pressure ratio p/p_0 is 13.2 in Fig. 9. The time path of relatively lower peak values exhibits a wavy profile at the right-hand side from the stagnation point. The system of values indicates that a pulsating and vortical supersonic shear layer strongly disturbed by the unsteady supersonic jet is streaming downward.

Unsteady flow characteristics obtained in the case of $\theta = 0$ deg is explained next. The result of this case might show an intermediate form between type IV and type VII. The supersonic jet does not strike the body strongly. However, it induces a relatively strong vortical supersonic shear layer. The supersonic jet seems to be transformed directly into the supersonic shear layer. Figure 10 shows the instantaneous pressure contours. Periodical compression waves generating from the edge of the supersonic shear layer are observed. This periodicity is also confirmed from Fig. 11, which plots the time history of the pressure ratio cross $\xi = \text{const}$ line defined in Fig. 2. From Fig. 10, other peak contours moving downward from the bow shock in Fig. 7b should be contact discontinuities due to the interaction with the compression wave. The unsteady flow characteristic of these compression waves and contact discontinuities is quite similar to that in Fig. 3 and Ref. 7. The time history of the pressure ratio distributions on the body surface is plotted in Fig. 12. The maximum pressure ratio $p/p_0 = 7.9$ is relatively small compared with the case of $\theta = -11$ deg. However, a high-pressure region is found at the left-hand side of the stagnation point of the jet. It might push the supersonic jet toward the upper downstream region in Fig. 7b. The influence of small periodical shocklet/vortex interactions in the supersonic shear layer found in Fig. 7b is also plotted as periodical peaks at the region of the supersonic shear layer in Fig. 12. The shocklet structure might be formed when the jet bow shock at the stagnation point is turned toward the upper side according to the jet oscillation.

The results of the third case at $\theta = 15$ deg are explained. Figures 13, 14, and 15 show the instantaneous contours of pressure, vibrational temperature, and N_2 mass fraction, respectively. Separate shocklets or compression waves, corresponding to those in Fig. 7c, are also found in Fig. 13. The vibrational temperature

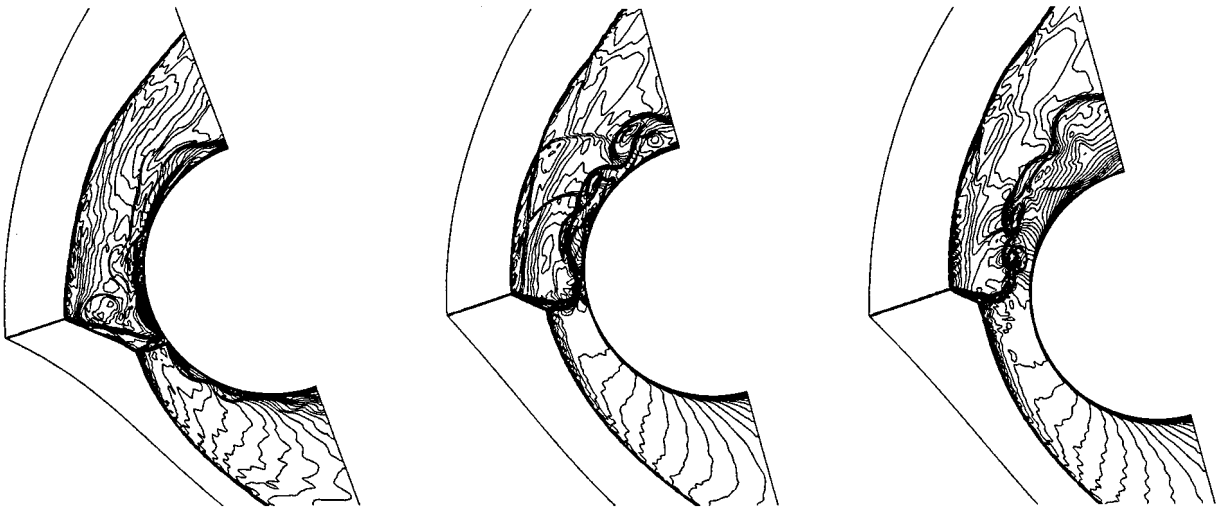

Fig. 7 Instantaneous translational-rotational temperature contours.

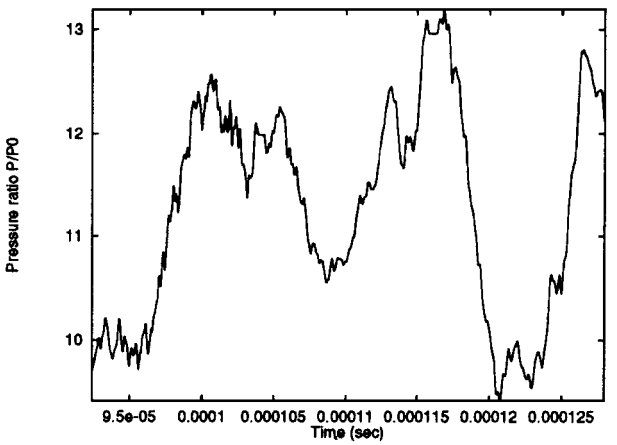

Fig. 8 Time history of the maximum pressure ratio on the body surface.

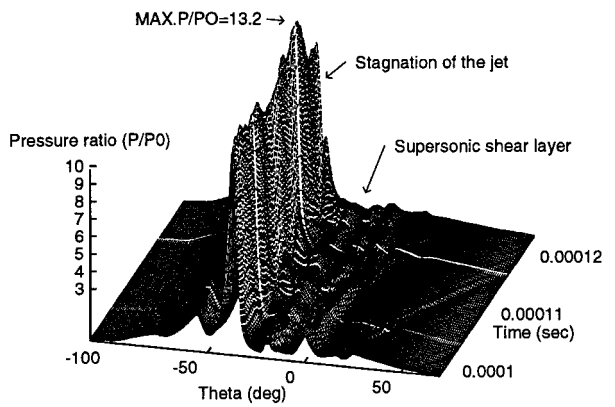

Fig. 9 Time history of the pressure ratio distributions on the body surface.

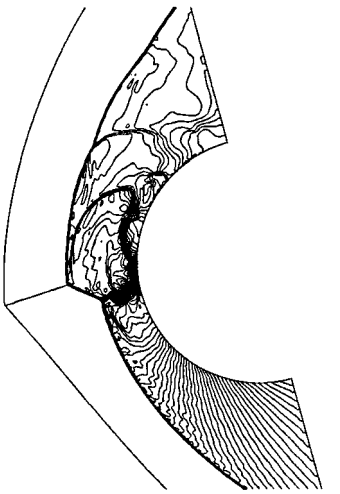

Fig. 10 Instantaneous pressure contours.

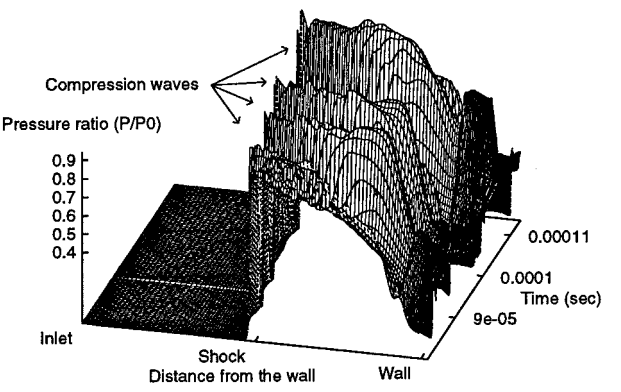

Fig. 11 Time history of pressure ratio cross ξ = const line.

is relatively low in the supersonic jet in Fig. 14. This is explained by Fig. 15, where only a sight dissociation of N_2 occurs in the supersonic jet. Figures 13–15 all demonstrate a vortical supersonic jet. The flow mechanisms in Figs. 13–15 are summarized in Fig. 16 and are explained systematically to understand the system of the mechanisms. The flowfield may be divided into six regions, A–F. Region A is a subsonic flowfield between the bow shock and the supersonic jet. Because a finite rate of N_2 dissociation occurs, the translational-rotational temperature and the vibrational temperature are highly increased. Region B, between the supersonic jet and the upper body surface, becomes a supersonic flow accelerated by the jet except for the boundary layer. Region C is another subsonic flowfield at the lower side. The flow characteristic in this region is simpler than that of the upper side. The dissociation of N_2 behind the bow shock also occurs in a finite rate, and both translational-rotational and vibrational temperatures are increased. Because the pressure in region C is relatively higher than that in region B, similar to the case of $\theta = 0$ deg, the supersonic jet is forced to stream toward the upper downstream region. Region D is located in the supersonic jet. Small shocklets, which may be similar to the well-known characteristic in

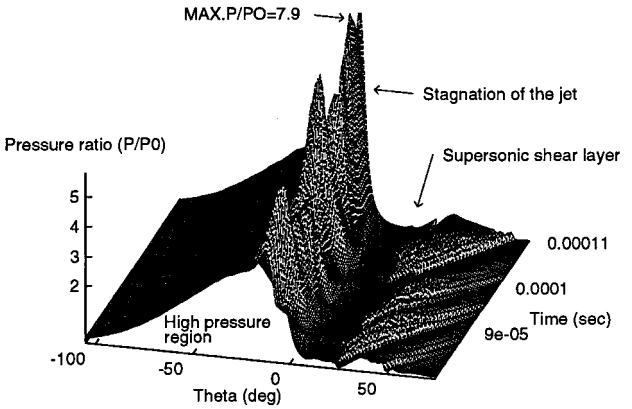

Fig. 12 Time history of the pressure ratio distributions on the body surface.

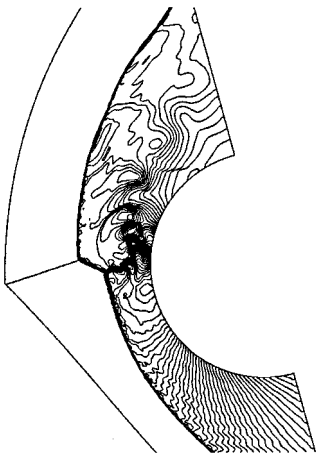

Fig. 13 Instantaneous pressure contours.

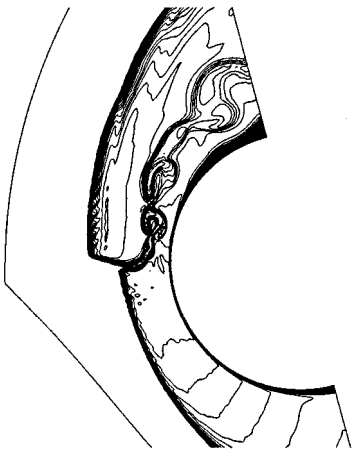

Fig. 14 Instantaneous vibrational temperature contours.

the supersonic exhaust gas ejecting from the jet engine outlet, are found along the jet. The strength is gradually weakened downward. In this region, because both translational-rotational and vibrational temperature increase slightly, the flow is almost frozen. Regions A and B are divided by the frozen flow. A quite unique flow structure is found in regions E and F. Region E is formed after the passage of a compression wave originally generated from a vortex edge of the vortical supersonic jet. Because the pressure in region D is lower than that in region E, the dissociation air in region A is pushed into region D. Finally, a fin shape region, region F, is formed. Consequently, this instability might be an essential flow mechanism in making a strongly vortical supersonic jet.

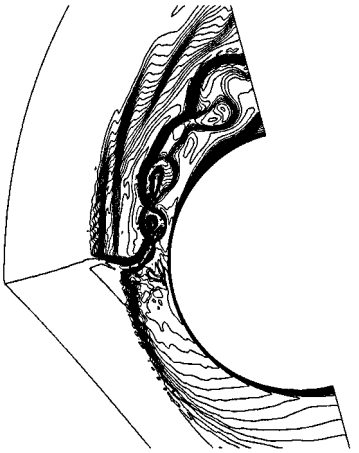

Fig. 15 Instantaneous N_2 mass fraction contours.

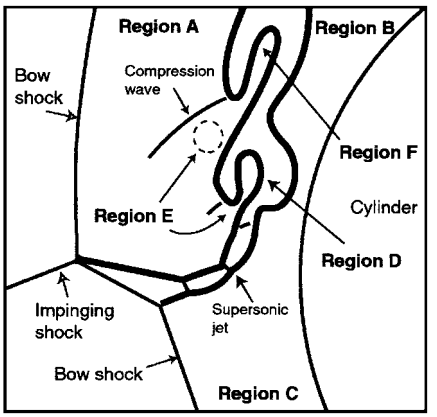

Fig. 16 Unsteady flow characteristics in θ = 15 deg case.

Concluding Remarks

Hypersonic shock/shock interference flows were calculated considering the thermochemical nonequilibrium effect, and unsteady and complicated flow characteristics were successfully obtained using the present CFD approaches. The results of the present study are summarized as follows:

1) The transition point of the shock/shock interference type from type IV to type III in the nonreaction cases is accurately evaluated by a parametric study changing the impinging shock location.

2) Unsteady flow characteristics, such as the unsteady supersonic jet, unsteady vortical supersonic shear layers, periodical compression waves, and induced contact discontinuities already reported in a previous study,[7] were also captured in the present study in the nonreaction cases.

3) The shock standoff distance decreases considerably in the reaction cases, and it results in the change of the shock/shock interference type.

4) Because the decrement of the shock standoff distance increases the pressure at the lower flow region defined as region C in Fig. 16, the supersonic jet is turned toward the upper downstream region in the cases of $\theta = 0$ and 15 deg.

5) Complicated unsteady flow characteristics, similar to the nonreaction cases, such as vortical supersonic shear layers, compression waves, and contact discontinuities, were also captured in the reaction cases.

6) A new type of shock/shock interference, that of a supersonic jet streaming toward the upper downstream without stagnating on the body, was obtained in the reaction case of $\theta = 15$ deg.

7) The supersonic jet became a strongly vortical flow due to the production of compression waves from the vortex edge of the jet itself.

Finally, the present CFD approach, the SSR, would be a useful tool for understanding unsteady flow characteristics of the shock/shock interference flow with the thermochemical nonequilibrium effect.

Accurate evaluations such as the heat transfer rate in the actual air should be studied next.

Acknowledgments

The computation was performed on the NEC SX-4/2C in our laboratory. The authors wish to thank C. Park of Tohoku University (now of NASA Ames Research Center) for his lecture on the chemical reaction model and also X. Zhong of the University of California, Los Angeles, for the copy of his new paper.

References

[1]Edney, B. E., "Anomalous Heat Transfer and Pressure Distributions on Blunt Bodies at Hypersonic Speeds in the Presence of an Impinging Shock," Aeronautical Research Inst. of Sweden, FFA Rept. 115, Stockholm, Sweden, Feb. 1968.

[2]Hains, F. D., and Keyes, J. W., "Shock Interference Heating in Hypersonic Flows," *AIAA Journal*, Vol. 10, No. 11, 1972, pp. 1441–1447.

[3]Wieting, A. R., and Holden, M. S., "Experimental Shock-Wave Interference Heating on a Cylinder at Mach 6 and 8," *AIAA Journal*, Vol. 27, No. 11, 1989, pp. 1557–1565.

[4]Holden, M., and Kolly, J., "Measurements of Heating in Regions of Shock/Shock Interaction in Hypersonic Flow," AIAA Paper 95-0640, Jan. 1995.

[5]Lind, C. A., and Lewis, M. J., "Unsteady Characteristics of a Hypersonic Type IV Shock Interaction," *Journal of Aircraft*, Vol. 32, No. 6, 1995, pp. 1286–1293.

[6]Zhong, X., "Application of Essentially Nonoscillatory Schemes to Unsteady Hypersonic Shock–Shock Interference Heating Problems," *AIAA Journal*, Vol. 32, No. 8, 1994, pp. 1606–1616.

[7]Yamamoto, S., and Kano, S., "Structure of Bow Shock and Compression Wave Interactions in Unsteady Hypersonic Shock/Shock Interference Flow," AIAA Paper 96-2152, June 1996.

[8]Kortz, S., McIntyre, T. J., and Eitelberg, G., "Experimental Investigation of Shock-on-Shock Interactions in the High-Enthalpy Shock Tunnel Göttingen (HEG)," *Proceedings of the 19th International Symposium on Shock Waves*, Vol. 1, Springer–Verlag, Berlin, 1993, pp. 75–80.

[9]Hornung, H. G., Cummings, E. B., Germain, P., Sanderson, S. R., Sturtevant, B., and Wen, C.-Y., "Recent Results from Hypervelocity Research in T5," AIAA Paper 94-2523, June 1994.

[10]Hannemann, K., Brück, S., and Brenner, G., "Numerical Simulation of Reacting Flows Related to the HEG," *Proceedings of the 19th International Symposium on Shock Waves*, Vol. 2, Springer–Verlag, Berlin, 1993, pp. 252–256.

[11]Furumoto, G. H., Zhong, X., and Skiba, C., "Numerical Studies of Real-Gas Effects on Two-Dimensional Hypersonic Shock-Wave/Boundary-Layer Interaction," *Physics of Fluids*, Vol. 9, No. 1, 1997, pp. 191–210.

[12]Nagatomo, H., Yamamoto, S., and Daiguji, H., "Numerical Investigation of Shock Interference in Hypersonic Thermochemical Nonequilibrium Flow," *Proceedings of the Third ECCOMAS Computational Fluid Dynamics Conference*, Wiley, New York, 1996, pp. 39–44.

[13]Gnoffo, P. A., "Upwind-Biased, Point-Implicit Relaxation Strategies for Viscous Hypersonic Flows," AIAA Paper 89-1972, 1989.

[14]Candler, G. V., and MacCormack, R. W., "Computation of Weakly Ionized Hypersonic Flows in Thermochemical Nonequilibrium," *Journal of Thermophysics and Heat Transfer*, Vol. 5, No. 3, 1991, pp. 266–273.

[15]Park, C., and Yoon, S., "Fully Coupled Implicit Method for Thermochemical Nonequilibrium Air at Suborbital Flight Speeds," *Journal of Spacecraft and Rockets*, Vol. 28, No. 1, 1991, pp. 31–39.

[16]Park, C., "Two-Temperature Interpretation of Dissociation Rate Data for N_2 and O_2," AIAA Paper 88-0458, Jan. 1988.

[17]Park, C., "Review of Chemical-Kinetic Problems of Future NASA Missions, I: Earth Entries," *Journal of Thermophysics and Heat Transfer*, Vol. 7, No. 3, 1993, pp. 385–398.

[18]Wada, Y., and Liou, M.-S., "A Flux Splitting Scheme with High-Resolution and Robustness for Discontinuities," AIAA Paper 94-0083, Jan. 1994.

[19]Eberhardt, S., and Imlay, S., "Diagonal Implicit Scheme for Computing Flows with Finite Rate Chemistry," *Journal of Thermophysics and Heat Transfer*, Vol. 6, No. 2, 1992, pp. 208–216.

[20]Blottner, F. G., Johnson, M., and Ellis, M., "Chemically Reacting Viscous Flow Program Multi-Component Gas Mixtures," Sandia Lab., Rept. SC-RR-70-754, Albuquerque, NM, 1971.

[21]Lee, J. H., "Basic Governing Equations for the Flight Regimes of Aeroassisted Orbital Transfer Vehicles," *Thermal Design of Aeroassisted Orbital Transfer Vehicles*, Vol. 96, Progress in Aeronautics and Astronautics, AIAA, Washington, DC, 1985, pp. 3–55.

[22]Liou, M.-S., and Steffen, C. J., "A New Flux Splitting Scheme," *Journal of Computational Physics*, Vol. 107, No. 1, 1993, pp. 23–39.

[23]Yamamoto, S., and Daiguji, H., "Higher-Order-Accurate Upwind Schemes for Solving the Compressible Euler and Navier–Stokes Equations," *Computers and Fluids*, Vol. 22, No. 2/3, 1993, pp. 259–270.

[24]Lobb, R. K., "Experimental Measurement of Shock Detachment Distance on Spheres Fired in Air at Hypervelocities," *The High Temperature Aspects of Hypersonic Flow*, 1964, Pergamon, New York, pp. 519–527.

[25]Hornung, H. G., "Non-Equilibrium Dissociating Nitrogen Flow over Spheres and Circular Cylinders," *Journal of Fluid Mechanics*, Vol. 53, No. 1, 1972, pp. 149–176.

[26]Yamamoto, S., Nagatomo, H., and Daiguji, H., "An Implicit-Explicit Flux Vector Splitting Scheme for Hypersonic Thermochemical Nonequilibrium Flows," *Proceedings of 14th International Conference on Numerical Methods in Fluid Dynamics*, Vol. 453, Lecture Notes in Physics, Springer–Verlag, Berlin, 1994, pp. 314–319.

B. A. Bhutta
Associate Editor